# Title

**The Bioelectrics of Immortality and Mortality in Cold-Sensitive *Hydra oligactis***

# Authors

Stefania E. Kapsetaki[1], Michael Levin[1,2,3,*]

# Affiliations

[1] Department of Biology, Tufts University, Medford, MA 02155, United States
[2] Allen Discovery Center at Tufts University, Medford, MA 02155, United States
[3] Wyss Institute for Biologically Inspired Engineering, Harvard University, Boston, MA 02115, United States
* Corresponding author
E-mail: michael.levin@allencenter.tufts.edu

# Keywords:

bioelectric map, bioelectric atlas, cnidaria, hydrozoa, bioelectric pattern, membrane voltage, Vmem, resting potential

# Running title:

Bioelectrics of Hydra

# Abstract

Bioelectric properties of cells are an important aspect of development, regeneration, and cancer. Because of their relevance to establishment and maintenance of tissue form and function, bioelectric patterns have been hypothesized to have a role in aging. However, no data on bioelectric patterns of the whole body of young and old individuals have been available. We observed and quantified the bioelectrics of whole-body immortal (growing at 22°C) and aging mortal (growing at 10°C) cold-sensitive (CS) *Hydra oligactis*. We found that the membrane-voltage-sensitive dyes FluoVolt and VF2.1.Cl can be used to reveal large-scale patterns of cellular membrane resting voltage potentials in Hydra. The consensus whole-body bioelectric atlas of immortal *H. oligactis* shows a consistently depolarized foot, and occasionally depolarized tentacles. Immortal hydra are on average more depolarized and exhibit less sharply-defined bioelectric patterns than old mortal hydra. Immortal hydra have a sharper foot:central body ratio than old mortal hydra. These data establish hydra as the first model system in which whole-body bioelectric imaging can be performed; the different bioelectric patterns of immortal versus old mortal hydra are consistent with a bioelectric component to the aging process and suggest a roadmap for using this model organism in anti-aging therapeutic screens involving electroceuticals.

# Introduction

Aging presents as a severe, progressive reduction in functional capacity and quality of life with a 100% penetrance [1, 2]. It also presents fascinating fundamental questions in evolutionary, cell, and developmental biology with respect to the algorithms implemented by living tissues to maintain form and function against disorder [3-12]. Numerous theories of the underlying molecular causes of aging have been proposed [13-21]. One set of approaches focuses on the progressive degradation of developmental information – cues that allow tissues to maintain a complex morphology for decades while materials and individual cells move in and out of the body. Since one key aspect of this information structure is maintained in bioelectrical gradients of resting potential across tissues (reviewed in [22-24]), it has been suggested that degradation of specifically bioelectric information could be a cause of aging [25, 26].

Patterns of cellular resting potential ($V_{mem}$) have been measured in a variety of embryonic, regenerative, and oncogenic contexts [27-31], due to the known role of developmental bioelectricity in regulating morphogenesis and cancer suppression (reviewed in [22, 23]). However, no data are currently available on large-scale bioelectric profiles during aging in vivo in any model species. This is a rate-limiting step in the development of electroceuticals for longevity. Moreover, additional bioelectricity-relevant approaches involve applying specific electromagnetic fields and pulsed electromagnetic fields to slow down aging [32-34], performing transcranial direct current stimulation and transcranial magnetic stimulation to improve the declining cognitive functions [35, 36], regulating the body's ion channels with morphoceuticals [37, 38] or gero-electroceuticals [39], bioelectrically controlling stem cells such as their ability to differentiate or continue regenerating [40], and regulating the restoration of the body's aging bioelectrics with implantable and wearable bioelectronic devices [41]. Evaluating, improving, and extending these pioneering approaches require a better understanding of the bioelectric pattern of young versus old individuals. Thus, we sought to establish a dataset on whole-body bioelectric imaging in a model system that is relevant for aging research [42-44].

Hydra are relatively small fresh-water invertebrates. They have endodermal and ectodermal tissues, and can reproduce both sexually and asexually [45]. They have been used as a model organism in many studies [46] focusing on their development, regenerative abilities, transplantation biology [46], tumor biology [47-49], whole-body neural and muscle activity via calcium imaging [50-52], and aging [53, 54]. Their body is transparent, enabling membrane-voltage ($V_{mem}$)-sensitives dyes [55-57] to easily penetrate and reveal cellular membrane voltage of the whole organism. At 22°C, cold-sensitive (CS) *Hydra oligactis* are immortal. However, at 10°C, CS *H. oligactis* begin to switch to sexual reproduction and produce ovaries and testes within 3-4 weeks [58, 59]. Within 30 days at 10°, CS *H. oligactis* undergo aging [60] and eventually die by day 150 [60]. It is known that 80% of the human aging genes from the Human Ageing Genomic Resources (http://genomics.senescence.info) are conserved in hydra [54]. Aging CS *H. oligactis* are less able to grab prey, perform spontaneous contractions, and transfer food to their gut, have fewer sperm and nurse cells after 30 days, fewer numbers of interstitial stem cells, and more epithelial cells [60]. This makes hydra an ideal model system in which to begin to test hypotheses about the role of bioelectrics in the aging process. However, the bioelectrics of whole-body immortal and aging hydra are unknown.

We established an imaging protocol for this species and tested the hypothesis that bioelectric patterns (non-homogenous spatial distributions of $V_{mem}$) would exist, and would change with aging, especially becoming less crisp and more diffuse (degradation of prepattern as observed during some birth defects [61]). Moreover, we tested the prediction that aging CS *H. oligactis* would be more hyperpolarized than immortal CS *H. oligactis*.

# Methods

## Hydra husbandry and shrimp maintenance

We obtained CS *Hydra oligactis* from Brigitte Galliot's lab. We grew the hydra in media consisting of 0.294 g CaCl2, 0.07 g MgSO4, 0.08 g NaHCO3, and 0.004 g KCl per 2 L of DI water. We stored the hydra in 150 x 15mm plastic Petri dishes (maximum 50 hydra per dish) in a light:dark 16:8 h cycle incubator at 22°C. We transferred the hydra to a new Petri dish with fresh liquid approximately every 2 weeks. We grew artemia shrimps in a plastic cone oxygenated with an air pump in a light:dark 16:8 h cycle incubator at 22°C. The plastic cone had approximately 300 mL of artemia brine shrimp media (25 g NaCl and 0.5 g sodium bicarbonate per 1L of DI) and 0.5 g of artemia brine shrimp egg microcysts. We repeated the artemia brine shrimp growing process from artemia brine shrimp egg microcysts on Tuesdays and Fridays. We fed the hydra approximately 1-4 artemia brine shrimps per hydra on Mondays, Tuesdays, Thursdays, and Fridays.

## Aging induction

In the beginning of the experiment, after a month since the beginning, after two months since the beginning, and after three months since the beginning, we imaged four hydra from a CS *H. oligactis* culture growing at 22°C and four hydra from a CS *H. oligactis* culture growing at 10°C. After four months since the beginning of the experiment, we imaged eight hydra from the CS *H. oligactis* culture growing at 22°C and eight hydra from the CS *H. oligactis* culture growing at 10°C.

## Dyeing and imaging the hydra

We performed the following steps in order to dye and image the hydra. On the confocal microscope we set the chamber temperature at 18°C and 40% air flow. We used the 25X objective (HC Fluotar L Visir 25x/0.95 water) with drops of ultra-pure water on the objective. In the Leica Application Suite X (LASX) software we used the following settings: 1024 x 1024 dimensions; bidirectional mode turned on; line accumulation: 9; speed: 700 Hz; numerical aperture: 0.95; WLL ON at 85% and maximum power; PinholeAiry: 1AU; laser line (510 nm) and intensity 1.5%; spectral position: 528nm – 617nm; gain = 10.

We prepared the dye solution for multiple hydra on the day of imaging using 2mL-Eppendorf tubes. Specifically, we used the following volumes per hydra: FluoVolt (https://www.thermofisher.com/order/catalog/product/F10488) (0.5µL), powerload (https://www.thermofisher.com/order/catalog/product/P10020) (12.5µL), Neuro Background Suppressor 10X (12.5µL), and hydra media (224.5µL). We stored the Eppendorf tubes in the dark at room temperature until using them for each hydra in the next few hours. We collected the hydra from the 22°C incubator and then once finished imaging the 22°C hydra we imaged the hydra that were growing in the 10°C incubator. We placed a hydra in 250µL of the dye solution in a well of a 24-well plate. We set a timer for 5min. We then cut a cover slip on the sides so that it fitted in the middle of an ibidi dish (https://ibidi.com/35-mm-dishes/176--dish-35-mm-high-glass-bottom.html#/29-surface_modification-15h_170_m_5_m_d_263_m_schott_glass_sterilized/30-pcs_box-60_individually_packed). We placed mylokote glue on two opposite sides of the ibidi dish (enough glue so that the cover slip could later touch on both sides of the glue). Once the 5min had passed, we washed the well approximately 5 times with hydra media using a different plastic pipette each time. We collected the hydra with a plastic pipette and placed it in the middle of the ibidi dish. We placed the cover slip gently on top of the ibidi dish. We took a 10µL tip with the ibidi dish to the confocal microscope. We placed some additional ultra pure droplets on the confocal 25X objective if needed, so that the liquid touched the bottom of the ibidi dish. We started applying pressure on the sides of the cover slip where the mylokote glue until the mylokote glue did not

visibly move much further towards the center of the ibidi dish. We made sure the mylokote glue did not touch the hydra. We placed the ibidi dish on the confocal microscope stage. We switched the line repetitions on the LASX software to 1, went to tiling mode, and clicked on fast live. We focused on the surface of the hydra by adjusting the Z plane. We clicked on spiral and identified the whole body of the hydra. We stopped the spiral. Using the polygon tool, we selected the region of interest (the whole hydra). We turned the line repetitions to 9, clicked start, and on the image that was being processed we clicked on the "Pixel binding" option to convert it to 2. For every image we clicked on "fit", then "FLIM image fit", and used count threshold = 1. The maximum time that the hydra was being imaged under the confocal was 5 minutes. We then continued dyeing and then imaging the next hydra.

## Image analysis of the aging experiment

We obtained the mean lifetime intensity and brightness whole-body images of each FluoVolt-dyed hydra from the LASX software. We transferred these two images of each hydra on ImageJ. We also transferred and ran the following file (Supplementary File 1) on ImageJ. Downloading this file (Supplementary File 2) is also required. We then transferred and ran this file (Supplementary File 3) on ImageJ. In the case of the last file, we manually drew a line surrounding the hydra with the polygon tool. We used the rotation tool to rotate the hydra so that its anterior side was facing the left and its posterior side was facing the right. We then transferred and ran the following code on ImageJ (Supplementary File 4). The output values from ImageJ were mean lifetime intensity values across the whole body of the hydra. We transferred these values to Excel, calculated the mean value of the mean lifetime intensity, and the $1^{st}$ derivate of these values along the body of the hydra. We also measured the absolute value of the $1^{st}$ derivative, and the average of the absolute value of the $1^{st}$ derivative. The output values from ImageJ also provided values of the x axis (1 until the total length of the hydra). In order to normalize to the varied length of each hydra, we multiplied each position by 100/(the last x value of the hydra). For example, the last region of the hydra was the 100% region.

To compare the central region and foot region of the hydra we removed the tentacles by not selecting the tentacles when drawing a line around the hydra on ImageJ. We used the mean lifetime intensity data from the output of this ImageJ analysis and we divided the mean lifetime intensity of the last 4 regions of each hydra (approximately 83-100% of their body length) by the mean lifetime intensity of the region that was closest to 50% (of the body length of the hydra).

To measure bioelectric sharpness (Moran's I) of the whole-body of the hydra we transferred the mean lifetime intensity image of the hydra to ImageJ. We adjusted the brightness and contrast so that we could observe the edges of the hydra without applying those settings. Then we ran the following .lut file (Supplementary File 2). Then for each image, we cropped the region of interest (whole body of the hydra) using the polygon tool, and ran the following macros (Supplementary File 3). Then, we reset the brightness and contrast settings. We saved the image on the desktop as a TIFF format file. We then ran these two scripts (Supplementary files 5 & 6) in Idle [62].

## Consensus bioelectric map of the hydra

To make a bioelectric atlas/map of every hydra we analyzed separately the mean lifetime intensity whole-body data of the immortal hydra versus the mean lifetime intensity whole-body data of the old mortal hydra. We plotted the mean values of mean lifetime intensity of each hydra that was growing for 2 months (4 hydra), 3 months (4 hydra), and 4 months (8 hydra) at 22°C against the percentage of its body length on the x axis, and the mean values of mean lifetime intensity of each hydra that was growing for 2 months (4 hydra), 3 months (4 hydra), and 4 months (8 hydra) at 10°C against the percentage of its body length on the x axis.

## Image analysis of the VF2.0.Cl versus VF2.1.Cl and FluoVolt-dyed hydra

We dyed three three-and-a-half-month old CS *H. oligactis* for 5min with 250µL of the following solution (1.5µL of the VF2.1.Cl dye from a 1mM stock solution [63], 37.5µL powerload, 37.5µL Neuro Background Suppressor 10X, and 673.5µL hydra media). We dyed three three-and-a-half-month old CS *H. oligactis* for 5min with 250µL of the following solution (1.5µL of the VF2.0.Cl dye from a 1mM stock solution [63], 37.5µL powerload, 37.5µL Neuro Background Suppressor 10X, and 673.5µL hydra media). We dyed three three-and-a-half-month old CS *H. oligactis* for 5min with 250µL of the following solution (1.5µL of the FluoVolt dye, 37.5µL powerload, 37.5µL Neuro Background Suppressor 10X, and 673.5µL hydra media). We performed this procedure separately for each hydra. After the 5min exposure to the dye in a well of a 24-well plate, we washed the well 4-5 times with hydra media. We placed mylokote glue on two opposite sides of an ibidi dish and moved the hydra with a plastic pipette to the middle of the ibidi dish. We slowly applied pressure on the sides of the cover slip, where the mylokote glue was, and imaged the hydra under the confocal microscope using the LasX software and the 25X objective. We used the following settings for all three dyes: 1024 x 1024 dimensions; bidirectional mode turned on, line accumulation: 9; speed: 700 Hz; numerical aperture: 0.95; WLL ON at 85% and maximum power; and PinholeAiry: 1AU. For imaging the FluoVolt-dyed hydra we used laser line (510 nm) and intensity 1.5%; spectral position: 528nm – 617nm; and gain = 10. Whereas for imaging the VF2.1.Cl- and VF2.0.Cl-dyed hydra we used laser line (510 nm) and intensity 30%; spectral position: 533nm – 622nm; and gain = 10. On the images that were being processed we clicked on the "Pixel binding" option to convert it to 2. Also, for every image we clicked on "fit", then "FLIM image fit", and used count threshold = 1.

We obtained the mean lifetime intensity and brightness whole-body images of the VF2.0.Cl- , VF2.1.Cl-dyed, versus FluoVolt-dyed hydra from the LASX software. We dragged these images on the ImageJ software. In the brightness image of each hydra, we looked for 6 neighboring cells in the foot region, and drew a circle around them in the mean lifetime intensity image to measure the average mean lifetime intensity of that region. We also found 6 neighboring cells from the middle region of brightness image of the hydra with maximum ±1 difference in brightness intensity. We drew a circle around those cells in the same position in the mean lifetime intensity image in order to measure the average mean lifetime intensity of those cells. We then compared the average mean lifetime intensity values of those two regions across the different conditions (VF2.0.Cl- versus VF2.1.Cl-dyed versus FluoVolt-dyed hydra).

## Statistical analyses

We performed all statistical analyses in R version 4.4.0 [64]. When the data followed an approximately normal distribution (*P*-value > 0.05 in Shapiro's test [65]) and we were comparing three or more different groups, we used an Analysis of Variance (ANOVA) test. If the data did not follow a normal distribution (*P*-value < 0.05 in Shapiro's test [65]) and we were comparing three or more different groups, we performed the Kruskal-Wallis test [66]. When the data did not follow a normal distribution (*P*-value > 0.05 in Shapiro's test [65]) and we were comparing two different groups, we performed the Wilcoxon rank sum exact test [67, 68].

# Results

## $V_{mem}$-sensitive dye reveals relative membrane voltage of every cell along the hydra's body

In order to determine whether we can use immortal and mortal CS *H. oligactis* as a model system to see the relative membrane voltage of every cell, we ran an imaging protocol with the $V_{mem}$-sensitive dye FluoVolt. We were able to see the relative membrane voltage of every cell in alive immortal and mortal CS *H. oligactis* (Supplementary Figure 1). Depending on the CS *H. oligactis'* body contraction or expansion at the exact time point of imaging, some cells appeared more elongated (e.g., anterior-right region of the hydra in Supplementary Figure 1A), while other cells appeared less elongated (e.g., anterior-right region of the hydra Supplementary Figure 1B). Therefore, our dyeing technique can reveal the whole-body bioelectric atlas of immortal and mortal CS *H. oligactis*.

## $V_{mem}$-sensitive dyes FluoVolt and VF2.1.Cl show relative membrane voltage and not artifacts

In order to test whether the $V_{mem}$-sensitive dyes FluoVolt and VF2.1.Cl do report relative membrane voltage of CS *H. oligactis* cells, we compared the average arrival time of old mortal CS *H. oligactis* dyed with FluoVolt, VF2.1.Cl, or the $V_{mem}$-*insensitive* dye VF2.0.Cl. In old mortal CS *H. oligactis* dyed with FluoVolt (N = 3) or VF2.1.Cl (N = 3) we saw that the average arrival time of the foot region was longer than the average arrival time of the central body region. However, in old mortal CS *H. oligactis* dyed with the $V_{mem}$-insensitive dye VF2.0.Cl (N = 3), the foot and central body regions had on average a similar average arrival time (Figure 1). The absence of the characteristic voltage pattern when using the closely-related but voltage-unresponsive VF2.0.Cl dye suggests that the signals we reported indeed show relative membrane voltage of hydra cells and unlikely to be due to artifacts unrelated to voltage.

## Immortal hydra have bioelectrically distinct body parts

In order to find the consensus bioelectric atlas of immortal CS *H. oligactis*, we imaged CS *H. oligactis* growing at 22°C with the $V_{mem}$-sensitive dye FluoVolt. We saw that the majority of immortal hydra had a depolarized foot. Some immortal hydra had depolarized tentacles. Other regions of the immortal hydra did not have such consistent membrane voltage among different individuals. For example, the mouth region and central body of the hydra varied in membrane voltage among the different individuals (Figure 2; N = 6). Therefore, the consensus whole-body bioelectric atlas of immortal hydra showed some consistently bioelectrically distinct regions, such as the depolarized foot, and some bioelectrically variable regions, such as the depolarized tentacles, the mouth, and central body.

## Cold-Sensitive *H. oligactis* age at 10°C

In order to confirm whether CS *H. oligactis* age at 10°C, we looked for ovaries or testes on the body of the hydra since gametogenesis in these hydra is a sign of irreversible aging [59, 69]. CS *H. oligactis* that had been growing for 78 days at 10°C had visible ovaries/testes (Supplementary Figure 2). Therefore, we conclude that in our assays, CS *H. oligactis* do indeed age at 10°C.

## Aging hydra have bioelectrically different bodies than immortal hydra

In order to test whether aging and immortal hydra have bioelectrically distinct bodies, we grew cultures of CS *H. oligactis* in 10°C versus 22°C incubators for 4 months and imaged the relative membrane voltage across the hydras' bodies using the $V_{mem}$-sensitive dye FluoVolt. The technical replicates, i.e., two whole-body images from the same individual, varied in mean lifetime intensity (Table 1). Both groups, the

technical replicates of the immortal and old mortal hydra, had similar standard deviations (Table 1: 4-46 picoseconds in the case of immortal hydra, and 4-47 picoseconds in the case of old mortal hydra). By analyzing one image of the whole body of each hydra, the standard deviation among the biological replicates of Figure 3 and Figure 4A was 101 picoseconds in the case of immortal hydra and 79 picoseconds in the case of old mortal hydra. We saw that the bodies of old mortal CS *H. oligactis*, that had been growing for 2, 3, or 4 months at 10°C, were on average more hyperpolarized ($N_{immortal}$ = 16, $N_{old\ mortal}$ = 16; Figure 3; Figure 4A: $p < 0.0001$) and bioelectrically sharper ($N_{immortal}$ = 16, $N_{old\ mortal}$ = 16; Figure 4B; $p = 0.03$) than immortal CS *H. oligactis,* that had been growing for 2, 3, or 4 months at 22°C. The foot-to-central body ratio of old mortal hydra was not as bioelectrically sharp as that of immortal hydra ($N_{immortal}$ = 16, $N_{old\ mortal}$ = 16; Figure 5; $p = 0.01$). Therefore, the bodies of old mortal and immortal hydra have distinct average relative membrane voltage and sharpness of different body regions.

# Discussion

This study provides a consensus whole-body bioelectric atlas of living immortal and mortal CS *H. oligactis*. We confirmed that CS *H. oligactis* were aging at 10°C since they had formed ovaries/testes within 78 days, an indication that this strain is undergoing irreversible aging [59, 69].

Our results showed that in this model system, the FluoVolt and VF2.1.Cl dyes were showing $V_{mem}$ of the plasma membrane and not artifacts, as revealed by the lack of signal from a closely-related control dye that is not responsive to membrane potential. This control has been used in cultures of rat hippocampal neurons, human cardiomyocytes, human embryonic kidney cells [70-72], and the tails of alive frog embryos [73], but is not common and should be universally used in voltage dye studies.

Prior efforts have mapped action potentials of the anterior region of the guinea pig's heart (e.g., [74, 75]), resting potential patterns in bacterial biofilms [76], central regions of poplar leaves [77] and stem and leaf of sunflowers *Helianthus annuus* [78], the optic tectum region of the frog brain [79], the olfactory bulb of the salamander *Ambystoma tigrinum* [80, 81], faces, brains, and tails of frog embryos [30, 73, 82], olfactory bulb of zebrafish [83, 84], olfactory bulb of box turtles *Terepene triunguis* [85], an embryonic precontractile chick heart [86], the pig heart [87], mouse heart [75, 88], and the primary somatosensory cortex of the mouse brain [89]. We show for the first time the relative membrane voltage of alive cells across the whole body of 38 whole organisms. Certain properties of hydra and technological advances have made this possible. Specifically, the transparency of hydra has enabled $V_{mem}$-sensitive dyes to easily penetrate the hydra and be observed under the confocal microscope using FLIM that shows the relative membrane voltage of each cell.

One of the key aspects of bioelectric patterns is that in some systems (Xenopus embryo, regenerating planaria, chick embryo), their distribution has been shown to serve as an instructive signal for morphogenesis [30, 90-93]. Thus, we were very interested in differences in $V_{mem}$ across the hydra that would correspond to distinct anatomical features. We found that the CS *H. oligactis* foot was more depolarized than other regions of the hydra's body. The tentacles of the CS *H. oligactis* were also relatively depolarized in some individual hydra. This relative depolarization may relate to the adhesive properties of the foot and secretory properties of the hydra's tentacles. The hydra's foot (also called basal disc) secretes granules that contain glycans and/or glycoproteins allowing the hydra to stick on surfaces [94]. Although the resting membrane potential of the secretory cells of the foot has not been previously reported, other secretory cells, called nematocytes, in the tentacles of *Hydra vulgaris* are known to require apical plasma membrane depolarization for the secretion of stenoteles [95].

As with any biological parameter, we observed some variability across animals. The standard deviation in mean lifetime intensity was higher among the biological than among the technical replicates. Specifically, the standard deviation in mean lifetime intensity among the biological replicates of the data

shown in Figure 3 and Figure 4A was 101 and 79 picoseconds in the case of the immortal hydra and old mortal hydra, respectively. Whereas the standard deviation in mean lifetime intensity among the technical replicates (N = 2; Table 1) was 4-46 picoseconds in the case of four immortal hydra and 4-47 picoseconds in the case of four old mortal hydra. Although the standard deviation in mean lifetime intensity of the technical replicates was only measured from two technical replicates, the higher standard deviation in the case of the biological replicates than the technical replicates indicates that each hydra does not have the exact same whole-body mean lifetime intensity than other hydra. There tends to be more interindividual variation in the bioelectric pattern of hydra than temporal (1-3 minute) variation in the bioelectric pattern of a single individual. In other words, the lower standard deviation in the case of the technical replicates, versus biological replicates, indicates that data within the ~4-47 picosecond standard deviation could be considered temporal intraindividual variation ('noise') and data beyond the ~47 picosecond standard deviation could be considered interindividual variation ('signal'). Future work on the functional role of this parameter in Hydra biology will be necessary because it is the precision of interpretation of the voltage profile by body systems that would determines the degree of precision that is physiologically important.

One basic bioelectric parameter to compare in living samples is simply the overall average level of polarization. With respect to this, we found a more hyperpolarized bioelectric pattern in the whole body of old mortal than immortal hydra. What we found was reasonable for four reasons. First, we would expect the immortal hydra's foot and tentacles to be relatively depolarized, due to the depolarization required for excretion of substances in secretory cells present in those regions. If this depolarization becomes dysregulated during aging, we would expect old hydra to be on average more hyperpolarized than immortal CS *H. oligactis*. Second, interstitial stem cells give rise to several cell types, including secretory cells, nematocytes, nerve cells, and germ cells [96]. Interstitial stem cells decrease in numbers in aging hydra [96] and this may lead to a decrease in the interstitial-stem-cell-derived depolarization-activated nematocytes in aging hydra. Prior data connect resting potential to the maintenance of stem cells [97-100]. Third, stem cells are usually relatively depolarized [101], and the decrease in interstitial stem cells in aging hydra may mean that these hydra become more hyperpolarized. Fourth, hyperpolarization of the plasma membrane is known to determine actin fiber compaction in cultures of bovine epithelial cells [102], and actin fibers appear disrupted in aging *H. oligactis* [60]. Thus, although these two processes happen in very evolutionary distant species, the disrupted actin fibers of aging hydra may be due to cell hyperpolarization.

There seems to be some variety across organisms in terms of the relationship of polarization level to aging. For example, Type II neurons in the bed nucleus of the stria terminalis are more hyperpolarized in aged mice than young mice [103]. In rats, old versus young hippocampal CA1 neurons did not have significantly different resting membrane potentials [104]. Also, there was not a significant difference in the resting membrane potential of old versus young pyramidal neurons of the prefrontal cortex of rhesus monkeys [105]. In female and male mouse bladder cells, the mRNA expression of hyperpolarization-activated cyclic nucleotide-gated (HCN) channel hcn1 decreases with age [106]. If hnc1 expression is lower and production of HCN1 proteins is decreased in aging hydra, this may explain the potential inability of cells to maintain their depolarized state as they age, i.e. our finding that older mortal hydra are more hyperpolarized than immortal hydra.

In addition to average polarization, it is interesting to consider the crispness of the bioelectric pattern itself: the degree to which bioelectric patterns sharply distinguish compartments with different $V_{mem}$ [22, 107]. In embryos, a number of teratogens that disrupt developmental morphogenesis do so by making the bioelectric prepattern less sharp [61, 108]. For example, in the Xenopus brain this is known to be the case for chemical and genetic teratogens; crucially, brain morphogenesis, gene expression, and even learning rates can be restored despite exposure to nicotine, ethanol, or mutation of the Notch gene by artificially forcing the bioelectric pattern to become sharper (via overexpression of the HCN2 ion channel)

[109-111]. We previously suggested the hypothesis that aging could involve a change of the sharpness of the bioelectrical pattern [25] and indeed hcn1 expression decreases with age in mice [106]. We thus quantified here the sharpness of the bioelectrical patterns in immortal and aging hydra. We found a sharper bioelectric pattern in the whole body of old mortal than immortal hydra. However, the foot-to-central body ratio pattern was less sharp in old mortal hydra. This suggests that either different organisms handle this in different ways, or more likely, the relationship between crispness of $V_{mem}$ pattern and aging is not uniform across body regions.

Our work points to the need for numerous subsequent studies. In parallel with applying anti-aging bioelectric treatments (e.g., HCN2 overexpression) in hydra, it would be useful to understand the mechanisms underpinning the observed whole-body bioelectric atlas of hydra. What ion channels and pumps determine the membrane voltage of every cell? Are there particular groups of cells that have more coordinated/synchronized changes in membrane voltage than other more distant groups of cells in the hydra's body? How exactly are the known aging-related physiologies of hydra (decreased ability to capture prey, decreased ability to spontaneously contract and transfer food to the gut, fewer sperm and nurse cells after 30 days, fewer interstitial stem cells, and more epithelial cells [60]) associated with the bioelectric atlas of old mortal hydra? Relative hyperpolarization of the old hydra's body may also mean a hyperpolarization of the depolarization-activated nematocytes in the hydra's tentacles, thus contributing to their decreased ability to capture food. Stem cells are usually more depolarized than other cells [101], which may explain the relatively hyperpolarized body of old mortal hydra which are known to have fewer interstitial stem cells and more epithelial cells. However, the associations between the other old physiologies and the old mortal bioelectric atlas are largely unknown. The availability of protocols for generating transgenic hydra [112-115] suggest the possibility of using optogenetics and ion channel misexpression to understand the input of bioelectrics into hydra morphogenesis and aging. Likewise, it would be interesting to understand the role, if any, of endogenous bioelectrical states and the abilities of external alternating electric fields to induce reversal and continuation of hydra morphogenesis [116].

Identification of the whole-body bioelectric atlas of immortal and aging mortal hydra is a step towards performing similar studies in other model and non-model organisms. Studying the bioelectrics of aging in different taxa across the tree of life and the evolution of bioelectric pathways will help better understand the bioelectrics of aging in clinical settings. Examining the bioelectrics of human cells and tissues in both young and elderly populations would be essential in designing best practices for early human clinical trials using morphoceuticals [37] or gero-electoceuticals [39], i.e., drugs that target cellular bioelectrics and aim to reverse aging and aging-related diseases. Comparative developmental electrophysiology across widely distributed phyla is a first step in cracking the bioelectric code toward better understanding of evolutionary physiology and the biomedicine of aging and disease.

## Acknowledgements

We thank the Galliot lab for providing the cold-sensitive *Hydra oligactis*; Patrick McMillen for confocal training and advice on: culturing the hydra, imaging, dyeing, and VF2.1.Cl versus VF2.0.Cl image analysis; Erin Switzer for providing the artemia brine shrimps; Hamid Sediqi for sharing the code for calculating Moran's I, and to Parande Tayyebi, Patrick Erickson, Aviva Lucas-Demott, Alexandra Griffin, and Angelina Pimkina for help maintain the hydra.

## Funding

This research was supported by a sponsored research agreement from Astonishing labs.

## Competing Interests

M.L.'s lab has a sponsored research agreement with Astonishing Labs, a company seeking to advance the biomedicine of aging.

## Author Contributions

Conceptualization – ML, SK. Experimental design – ML, SK. Experiments and data gathering – SK. Data interpretation – ML, SK. Paper writing and editing – ML, SK.

## Figures

Figure 1

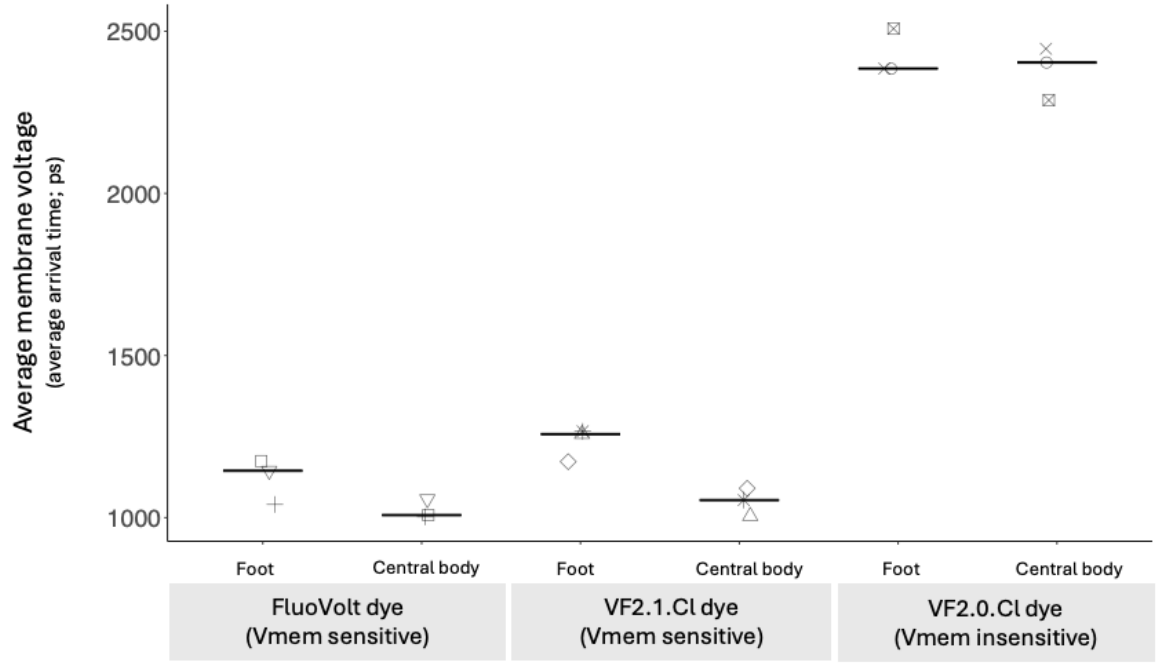


**Figure 1. The $V_{mem}$-sensitive dyes FluoVolt and VF2.1.Cl show membrane voltage, rather than $V_{mem}$-insensitive artifacts.** The y axis shows the average membrane voltage in foot or central body regions of 3 and a half month old cold-sensitive *H. oligactis* that have been growing at 10°C, dyed with the FluoVolt dye + powerload + Neurobackground suppressor, VF2.1.Cl dye + powerload + Neurobackground suppressor, or VF2.0.Cl dye + powerload + Neurobackground suppressor. The foot is relatively more depolarized than the middle part of the hydra's body when using the $V_{mem}$-sensitive dyes, but not when using the $V_{mem}$-insensitive dye. Same shapes are from the same hydra. There are three different hydra per dye condition. Crossbars show median values. ps: picoseconds.

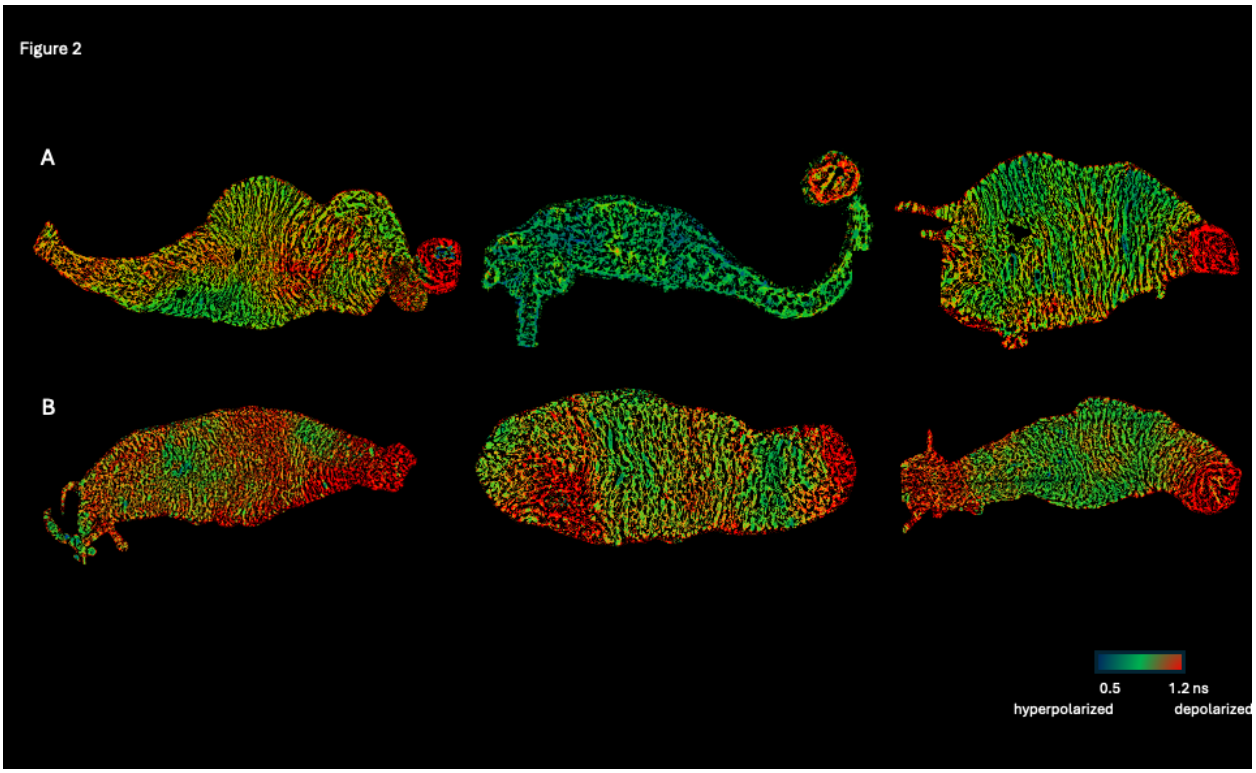


**Figure 2. The bioelectric atlas of different individual immortal cold-sensitive *H. oligactis* shows a common feature: a relatively depolarized foot and occasionally depolarized tentacles.** Examples of the relative membrane voltage of (A) three young cold-sensitive *Hydra oligactis* at 22°C; and (B) three 3-month young cold-sensitive *H. oligactis* at 22°C. Relative membrane voltage is observed using the FluoVolt dye. Mean lifetime intensity (ns) ranges from low (blue; hyperpolarized) to high (red; depolarized) values. ns: nanoseconds. Images analyzed in ImageJ software. We aligned the hydra so that their anterior is on the left and their posterior end is on the right.

Figure 3

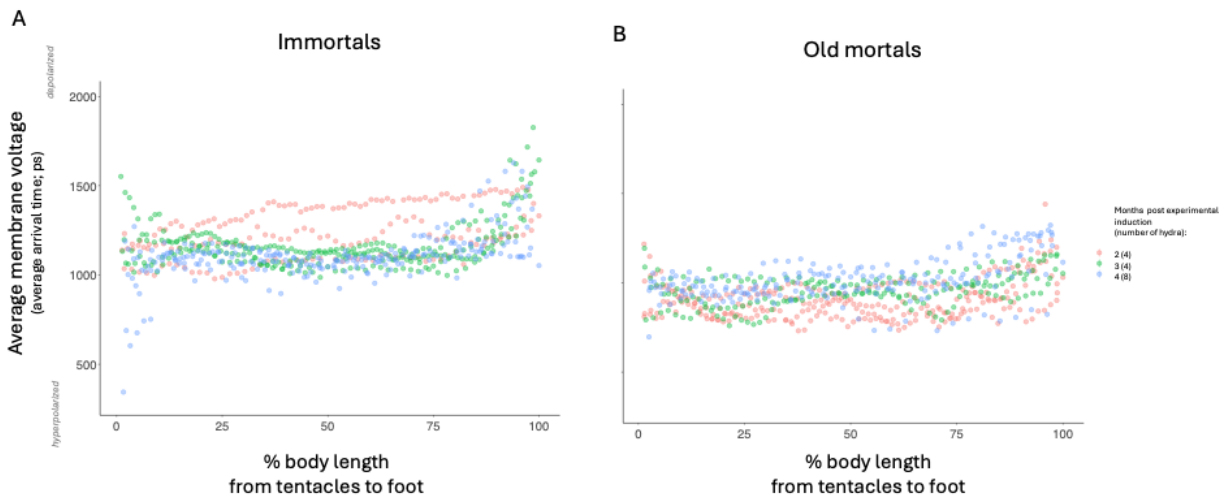


**Figure 3. The bioelectric atlas of 16 immortal cold-sensitive *H. oligactis* (A) is more depolarized on average, in the foot region, and occasionally in the tentacles in comparison to the bioelectric atlas of 16 old mortal cold-sensitive *H. oligactis* (B).** A and B have the same axes ranges. The mean lifetime intensities of the whole body of immortal hydra were not statistically different (Kruskal-Wallis test: *P*-value > 0.05) after 2 months (4 hydra), 3 months (4 hydra), or 4 months (8 hydra). Therefore, we show the mean lifetime intensity (A: y axis) from anterior to posterior (A: x axis) of these 16 different immortal hydra. The mean lifetime intensities of the whole body of old mortal hydra were not statistically different (ANOVA: *P*-value > 0.05) after 2 months (4 hydra), 3 months (4 hydra), or 4 months (8 hydra), therefore B shows the means of those 16 old mortal hydra. Therefore, we show the mean lifetime intensity (B: y axis) from anterior to posterior (B: x axis) of these 16 different old mortal hydra. ps: picoseconds.

Figure 4

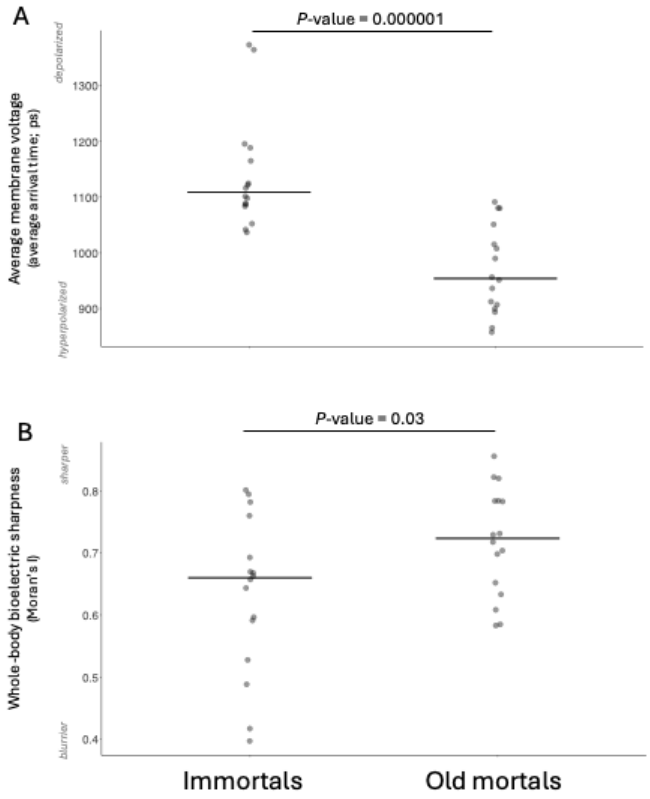


**Figure 4. The whole body of 16 old mortal hydra is on average more hyperpolarized (A) and bioelectrically sharper (B) than 16 immortal hydra.** (A) Average arrival time (ps) of the whole body of old mortal cold-sensitive *H. oligactis* (growing for 2, 3, or 4 months at 10°C; non-statistically significant difference between the average arrival time values between these three time points; ANOVA test: *P*-value > 0.05) versus immortal cold-sensitive *H. oligactis* (growing for 2, 3, or 4 months at 22°C; non-statistically significant difference between the average arrival time values between these three time points; Kruskal-Wallis test: *P*-value > 0.05). Sharpness (B) of the whole body of old mortal cold-sensitive *H. oligactis* (growing for 2, 3, or 4 months at 10°C; non-statistically significant difference between Moran's I values at these three time points; ANOVA test: *P*-value > 0.05) versus immortal cold-sensitive *H. oligactis* (growing for 2, 3, or 4 months at 22°C; non-statistically significant difference between Moran's I values at these three time points; ANOVA test: *P*-value > 0.05). Each point is a different CS *H. oligactis*. The hydra were dyed with the membrane voltage dye: FluoVolt. We only show p-values that are statistically different (P-value < 0.05). Result of Wilcoxon ran sum exact test (A): W = 242, p-value = $1.69 \times 10^{-6}$. Result of independent samples test (B): df = 26.7; P-value = 0.0374. The crossbars show medians. ps: picoseconds.

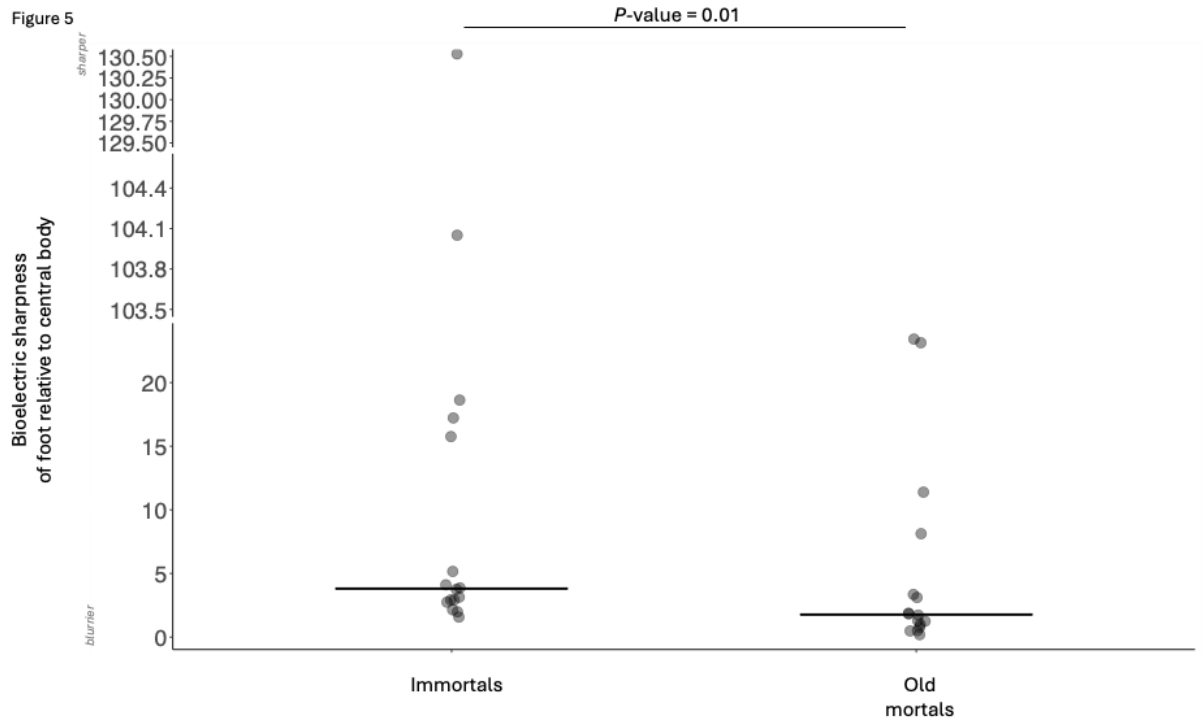


**Figure 5. The hydra's foot (relative to the bioelectric sharpness of its central body region) loses its bioelectric sharpness with age.** Each point is a different cold-sensitive *H. oligactis*. Sharpness of the foot relative to the central body of old mortal cold-sensitive *H. oligactis* (growing for 2, 3, or 4 months at 10°C; non-significant difference between the y values at these time points; Kruskal-Wallis test: *P*-value > 0.05) versus immortal cold-sensitive *H. oligactis* (growing for 2, 3, or 4 months at 22oC; non-significant difference between the y values at these time points; Kruskal-Wallis test: *P*-value > 0.05). The y axis is the median of the bioelectric sharpness of the foot region (approx. 83-100% of the hydra; where 100% is the edge of the foot) divided by the mean bioelectric sharpness of the middle region (approx. 50% position of body length of the hydra). The sharpness of the bioelectric pattern is the absolute value of the 1$^{st}$ derivative (of the mean lifetime intensity). Result of Wilcoxon rank sum exact test: W = 190, p-value = 0.01893. After removing the statistically significant outliers (Rosner's test), the statistical significance remains (two-samples t-test: t = 3.9266; df = 21; p-value = 0.0007). The crossbars show medians.

**Table 1.**

| Individual | Mean lifetime intensity (ps) | | Standard deviation (ps) among the two technical replicates | Time interval (min) between the 1st and 2nd technical replicate |
|---|---|---|---|---|
| | 1st technical replicate | 2nd technical replicate | | |
| 1st immortal hydra | 1009 | 1074 | 45.96 | 3 |
| 2nd immortal hydra | 1066 | 1125 | 41.72 | 3 |
| 3rd immortal hydra | 1061 | 1040 | 14.85 | 1 |
| 4th immortal hydra | 1124 | 1129 | 3.54 | 3 |
| 1st old mortal hydra | 1000 | 935 | 45.96 | 2 |
| 2nd old mortal hydra | 1003 | 977 | 18.38 | 3 |
| 3rd old mortal hydra | 1008 | 1013 | 3.54 | 1 |
| 4th old mortal hydra | 959 | 893 | 46.67 | 2 |

Legend: Technical replicates from the same individual vary in their bioelectrics.

These are examples of mean lifetime intensity values from technical replicate images of the whole body of four immortal hydra (4 months post experimental induction at 22°C) and four old mortal hydra (4 months post experimental induction at 10°C). Higher mean lifetime intensity values indicate relative depolarization, whereas lower mean lifetime intensity values indicate relative hyperpolarization. Longer duration of the hydra under the cover slip, i.e., longer time interval between the 1$^{st}$ and 2$^{nd}$ technical replicate, was not consistently an indication of depolarization or hyperpolarization. ps: picoseconds. min: minutes.

# Supplementary Material

**Supplementary Figure 1. Example images showing the relative membrane voltage across the anterior (left)-posterior (right) body of immortal (A: growing at 22°C) and mortal (B: growing at 10°C) cold-sensitive *H. oligactis*.** Mean lifetime intensity (ns) ranges from low (blue; hyperpolarized) to high (red; depolarized) values. We used the FluoVolt $V_{mem}$-sensitive dye to observe the relative membrane voltage. ns: nanoseconds.

**Supplementary Figure 2. Visible ovaries/testes (red arrows) in cold-sensitive *Hydra oligactis* growing for 78 days at 10°C, indicating that this strain ages at 10°C.** Image obtained with a Nikon SMZ1500 stereoscope.

**Supplementary Files 1-6.** Code for image analysis.

# References


1. Akushevich I, Kravchenko J, Akushevich L , et al. Medical cost trajectories and onsets of cancer and noncancer diseases in US elderly population. *Comput Math Methods Med* 2011;2011:857892. DOI: 10.1155/2011/857892.
2. Yashin AI, Stallard E, Land KC , et al. Medical cost trajectories and onset of age-associated diseases. *Biodemography of Aging: Determinants of Healthy Life Span and Longevity* 2016:143-162. DOI:
3. Sousounis K, Baddour JA, Tsonis PA. Aging and regeneration in vertebrates. *Curr Top Dev Biol* 2014;108:217-246. DOI: 10.1016/B978-0-12-391498-9.00008-5.
4. Miller WB, Jr., Baluska F, Reber AS , et al. Why death and aging ? All memories are imperfect. *Prog Biophys Mol Biol* 2024;187:21-35. DOI: 10.1016/j.pbiomolbio.2024.02.001.
5. Rubin H, Yao A, Chow M. Neoplastic development: paradoxical relation between impaired cell growth at low population density and excessive growth at high density. *Proc Natl Acad Sci U S A* 1995;92:7734-7738. DOI:
6. Rubin H. Mechanisms for enduring biological change. *Am J Physiol* 1992;262:L111-113. DOI:
7. Rubin H. What keeps cells in tissues behaving normally in the face of myriad mutations? *Bioessays* 2006;28:515-524. DOI: 10.1002/bies.20403.
8. Li S, Vazquez JM, Sudmant PH. The evolution of aging and lifespan. *Trends Genet* 2023;39:830-843. DOI: 10.1016/j.tig.2023.08.005.
9. Frankel S, Rogina B. Evolution, Chance, and Aging. *Front Genet* 2021;12:733184. DOI: 10.3389/fgene.2021.733184.
10. Meyer DH, Schumacher B. Aging clocks based on accumulating stochastic variation. *Nat Aging* 2024;4:871-885. DOI: 10.1038/s43587-024-00619-x.
11. Gems D, Singh Virk R, de Magalhães JP. Epigenetic clocks and programmatic aging. *Preprints* 2023. DOI: 10.20944/preprints202312.1892.v1.
12. de Magalhães JP. Programmatic features of aging originating in development: aging mechanisms beyond molecular damage? *FASEB J* 2012;26:4821-4826. DOI: 10.1096/fj.12-210872.
13. Gladyshev VN. On the cause of aging and control of lifespan: heterogeneity leads to inevitable damage accumulation, causing aging; control of damage composition and rate of accumulation define lifespan. *Bioessays* 2012;34:925-929. DOI: 10.1002/bies.201200092.
14. Gladyshev VN, Kritchevsky SB, Clarke SG , et al. Molecular Damage in Aging. *Nat Aging* 2021;1:1096-1106. DOI: 10.1038/s43587-021-00150-3.
15. Yang JH, Hayano M, Griffin PT , et al. Loss of epigenetic information as a cause of mammalian aging. *Cell* 2024;187:1312-1313. DOI: 10.1016/j.cell.2024.01.049.
16. Lu YR, Tian X, Sinclair DA. The Information Theory of Aging. *Nat Aging* 2023;3:1486-1499. DOI: 10.1038/s43587-023-00527-6.
17. Szilard L. On the Nature of the Aging Process. *Proc Natl Acad Sci U S A* 1959;45:30-45. DOI: 10.1073/pnas.45.1.30.
18. de Magalhães JP. Ageing as a software design flaw. *Genome Biol* 2023;24:51. DOI: 10.1186/s13059-023-02888-y.
19. Jin K. Modern Biological Theories of Aging. *Aging Dis* 2010;1:72-74. DOI:
20. Lipsky MS, King M. Biological theories of aging. *Dis Mon* 2015;61:460-466. DOI: 10.1016/j.disamonth.2015.09.005.
21. Gems D. The hyperfunction theory: An emerging paradigm for the biology of aging. *Ageing Res Rev* 2022;74:101557. DOI: 10.1016/j.arr.2021.101557.
22. Levin M. Bioelectric signaling: Reprogrammable circuits underlying embryogenesis, regeneration, and cancer. *Cell* 2021;184:1971-1989. DOI: 10.1016/j.cell.2021.02.034.

23. Bates E. Ion channels in development and cancer. *Annu Rev Cell Dev Biol* 2015;31:231-247. DOI: 10.1146/annurev-cellbio-100814-125338.
24. Harris MP. Bioelectric signaling as a unique regulator of development and regeneration. *Development* 2021;148. DOI: 10.1242/dev.180794.
25. Pio-Lopez L, Levin M. Aging as a loss of morphostatic information: A developmental bioelectricity perspective. *Ageing Res Rev* 2024;97:102310. DOI: 10.1016/j.arr.2024.102310.
26. Burr HS. The Problems of Ageing. *Yale J Biol Med* 1939;11:690-691. DOI:
27. Weiss I, Bohrmann J. Electrochemical patterns during Drosophila oogenesis: ion-transport mechanisms generate stage-specific gradients of pH and membrane potential in the follicle-cell epithelium. *Bmc Dev Biol* 2019;19:12. DOI: 10.1186/s12861-019-0192-x.
28. Kruger J, Bohrmann J. Bioelectric patterning during oogenesis: stage-specific distribution of membrane potentials, intracellular pH and ion-transport mechanisms in Drosophila ovarian follicles. *Bmc Dev Biol* 2015;15:1. DOI: 10.1186/s12861-015-0051-3.
29. Adams DS, Uzel SG, Akagi J , et al. Bioelectric signalling via potassium channels: a mechanism for craniofacial dysmorphogenesis in KCNJ2-associated Andersen-Tawil Syndrome. *J Physiol* 2016;594:3245-3270. DOI: 10.1113/JP271930.
30. Vandenberg LN, Morrie RD, Adams DS. V-ATPase-dependent ectodermal voltage and pH regionalization are required for craniofacial morphogenesis. *Dev Dyn* 2011;240:1889-1904. DOI: 10.1002/dvdy.22685.
31. Chernet BT, Levin M. Transmembrane voltage potential is an essential cellular parameter for the detection and control of tumor development in a Xenopus model. *Dis Model Mech* 2013;6:595-607. DOI: 10.1242/dmm.010835.
32. Perez FP, Zhou X, Morisaki J , et al. Engineered repeated electromagnetic field shock therapy for cellular senescence and age-related diseases. *Rejuvenation Res* 2008;11:1049-1057. DOI: 10.1089/rej.2008.0793.
33. Xu J, Liu K, Chen T , et al. Rotating magnetic field delays human umbilical vein endothelial cell aging and prolongs the lifespan of Caenorhabditis elegans. *Aging (Albany NY)* 2019;11:10385-10408. DOI: 10.18632/aging.102466.
34. Maredziak M, Tomaszewski K, Polinceusz P , et al. Static magnetic field enhances the viability and proliferation rate of adipose tissue-derived mesenchymal stem cells potentially through activation of the phosphoinositide 3-kinase/Akt (PI3K/Akt) pathway. *Electromagn Biol Med* 2017;36:45-54. DOI: 10.3109/15368378.2016.1149860.
35. Li S, Tang Y, Zhou Y , et al. Effects of Transcranial Direct Current Stimulation on Cognitive Function in Older Adults with and without Mild Cognitive Impairment: A Systematic Review and Meta-Analysis of Randomized Controlled Trials. *Gerontology* 2024;70:544-560. DOI: 10.1159/000537848.
36. Chen J, Wang Z, Chen Q , et al. Transcranial Direct Current Stimulation Enhances Cognitive Function in Patients with Mild Cognitive Impairment and Early/Mid Alzheimer's Disease: A Systematic Review and Meta-Analysis. *Brain Sci* 2022;12. DOI: 10.3390/brainsci12050562.
37. Pio-Lopez L, Levin M. Aging as a loss of morphostatic information: a developmental bioelectricity perspective. *Ageing Res Rev* 2024:102310. DOI: 10.1016/j.arr.2024.102310.
38. Pio-Lopez L, Levin M. Morphoceuticals: Perspectives for discovery of drugs targeting anatomical control mechanisms in regenerative medicine, cancer and aging. *Drug Discov Today* 2023;28:103585. DOI: 10.1016/j.drudis.2023.103585.
39. Tabibzadeh S, Brown OR. Trending toward gero-electroceuticals that target membrane potential for reprogramming aging and lifespan. *Aging and Cancer* 2024. DOI:
40. Sundelacruz S, Levin M, Kaplan DL. Membrane potential controls adipogenic and osteogenic differentiation of mesenchymal stem cells. *PloS one* 2008;3:e3737. DOI:

41. Huang Y, Yao K, Zhang Q , et al. Bioelectronics for electrical stimulation: materials, devices and biomedical applications. *Chemical Society Reviews* 2024. DOI:
42. Vogg MC, Buzgariu W, Suknovic NS , et al. Cellular, Metabolic, and Developmental Dimensions of Whole-Body Regeneration in Hydra. *Cold Spring Harb Perspect Biol* 2021;13. DOI: 10.1101/cshperspect.a040725.
43. Tomczyk S, Fischer K, Austad S , et al. Hydra, a powerful model for aging studies. *Invertebr Reprod Dev* 2015;59:11-16. DOI: 10.1080/07924259.2014.927805.
44. Reiter S, Crescenzi M, Galliot B , et al. Hydra, a versatile model to study the homeostatic and developmental functions of cell death. *Int J Dev Biol* 2012;56:593-604. DOI: 10.1387/ijdb.123499sr.
45. Lenhoff HM, Loomis WF. The biology of hydra and of some other coelenterates, 1961. 1961. DOI:
46. Galliot B. Hydra, a fruitful model system for 270 years. *Int J Dev Biol* 2012;56:411-423. DOI: 10.1387/ijdb.120086bg.
47. Domazet-Lošo T, Klimovich A, Anokhin B , et al. Naturally occurring tumours in the basal metazoan Hydra. *Nat Commun* 2014;5:4222. DOI: 10.1038/ncomms5222.
48. Boutry J, Mistral J, Berlioz L , et al. Tumors (re)shape biotic interactions within ecosystems: Experimental evidence from the freshwater cnidarian Hydra. *Sci Total Environ* 2022;803:149923. DOI: 10.1016/j.scitotenv.2021.149923.
49. Boutry J, Buysse M, Tissot S , et al. Spontaneously occurring tumors in different wild-derived strains of hydra. *Sci Rep* 2023;13:7449. DOI: 10.1038/s41598-023-34656-0.
50. Yuste R. Breaking the neural code of a cnidarian: Learning principles of neuroscience from the "vulgar" Hydra. *Curr Opin Neurobiol* 2024;86:102869. DOI: 10.1016/j.conb.2024.102869.
51. Szymanski JR, Yuste R. Mapping the Whole-Body Muscle Activity of Hydra vulgaris. *Curr Biol* 2019;29:1807-1817 e1803. DOI: 10.1016/j.cub.2019.05.012.
52. Dupre C, Yuste R. Non-overlapping Neural Networks in Hydra vulgaris. *Curr Biol* 2017;27:1085-1097. DOI: 10.1016/j.cub.2017.02.049.
53. Schenkelaars Q, Tomczyk S, Wenger Y , et al. Hydra, a model system for deciphering the mechanisms of aging and resistance to aging. In: *Conn's handbook of models for human aging*. (Elsevier). 2018; pp. 507-520.
54. Tomczyk S, Fischer K, Austad S , et al. Hydra, a powerful model for aging studies. *Invertebr Reprod Dev* 2015;59:11-16. DOI: 10.1080/07924259.2014.927805.
55. McMillen P, Levin M. Optical Estimation of Bioelectric Patterns in Living Embryos. *Methods Mol Biol* 2024;2745:91-102. DOI: 10.1007/978-1-0716-3577-3_6.
56. Adams DS, Levin M. Measuring resting membrane potential using the fluorescent voltage reporters DiBAC4(3) and CC2-DMPE. *Cold Spring Harb Protoc* 2012;2012:459-464. DOI: 10.1101/pdb.prot067702.
57. Adams DS, Levin M. General principles for measuring resting membrane potential and ion concentration using fluorescent bioelectricity reporters. *Cold Spring Harb Protoc* 2012;2012:385-397. DOI: 10.1101/pdb.top067710.
58. Martínez DE, Bridge D. Hydra, the everlasting embryo, confronts aging. *Int J Dev Biol* 2012;56:479-487. DOI: 10.1387/ijdb.113461dm.
59. Brien P. La PÉrennitÉ Somatique. *Biological Reviews* 2008;28:308-349. DOI: 10.1111/j.1469-185X.1953.tb01381.x.
60. Yoshida K, Fujisawa T, Hwang JS , et al. Degeneration after sexual differentiation in hydra and its relevance to the evolution of aging. *Gene* 2006;385:64-70. DOI: 10.1016/j.gene.2006.06.031.
61. Pai VP, Lemire JM, Pare JF , et al. Endogenous Gradients of Resting Potential Instructively Pattern Embryonic Neural Tissue via Notch Signaling and Regulation of Proliferation. *J Neurosci* 2015;35:4366-4385. DOI: 10.1523/JNEUROSCI.1877-14.2015.

62. Python Software Foundation. (n.d.). IDLE. .
63. Miller EW, Lin JY, Frady EP , et al. Optically monitoring voltage in neurons by photo-induced electron transfer through molecular wires. *Proc Natl Acad Sci U S A* 2012;109:2114-2119. DOI: 10.1073/pnas.1120694109.
64. Team RC. RA language and environment for statistical computing, R Foundation for Statistical. *Computing* 2020. DOI:
65. Shapiro SS, Wilk MB. An Analysis of Variance Test for Normality (Complete Samples). *Biometrika* 1965;52:591-611. DOI: 10.2307/2333709.
66. Kruskal WH, Wallis WA. Use of ranks in one-criterion variance analysis. *Journal of the American statistical Association* 1952;47:583-621. DOI:
67. Gibbons J, Chakraborti S. *Nonparametric Statistical Inference, 5th Revised Edn*. (Boca Raton, FL). 2011; 9781439896129.
68. Hollander M. *Nonparametric Statistical Methods*. (John Wiley & Sons Inc). 2013.
69. Tomczyk S, Buzgariu W, Perruchoud C , et al. Loss of Neurogenesis in Aging Hydra. *Dev Neurobiol* 2019;79:479-496. DOI: 10.1002/dneu.22676.
70. Boggess SC, Lazzari-Dean JR, Raliski BK , et al. Fluorescence lifetime predicts performance of voltage sensitive fluorophores in cardiomyocytes and neurons. *RSC Chem Biol* 2021;2:248-258. DOI: 10.1039/d0cb00152j.
71. Deal PE, Grenier V, Kulkarni RU , et al. Making life visible: Fluorescent indicators to probe membrane potential. In: *Make Life Visible*. Toyama Y, Miyawaki A, Nakamura M, et al., eds. (Springer, Singapore). 2020; pp. 89-104.
72. Lazzari-Dean JR, Gest AM, Miller EW. Optical estimation of absolute membrane potential using fluorescence lifetime imaging. *Elife* 2019;8. DOI: 10.7554/eLife.44522.
73. McMillen P, Levin M. Optical Estimation of Bioelectric Patterns in Living Embryos. *Methods Mol Biol* 2024;2745:91-102. DOI: 10.1007/978-1-0716-3577-3_6.
74. Efimov IR, Nikolski VP, Salama G. Optical imaging of the heart. *Circ Res* 2004;95:21-33. DOI: 10.1161/01.RES.0000130529.18016.35.
75. O'Shea C, Winter J, Kabir SN , et al. High resolution optical mapping of cardiac electrophysiology in pre-clinical models. *Sci Data* 2022;9:135. DOI: 10.1038/s41597-022-01253-1.
76. Prindle A, Liu J, Asally M , et al. Ion channels enable electrical communication in bacterial communities. *Nature* 2015;527:59-63. DOI: 10.1038/nature15709.
77. Fromm J, Lautner S. Electrical signals and their physiological significance in plants. *Plant Cell Environ* 2007;30:249-257. DOI: 10.1111/j.1365-3040.2006.01614.x.
78. Zhao DJ, Chen Y, Wang ZY , et al. High-resolution non-contact measurement of the electrical activity of plants in situ using optical recording. *Sci Rep* 2015;5:13425. DOI: 10.1038/srep13425.
79. Grinvald A, Anglister L, Freeman JA , et al. Real-time optical imaging of naturally evoked electrical activity in intact frog brain. *Nature* 1984;308:848-850. DOI: 10.1038/308848a0.
80. Orbach HS, Cohen LB. Optical monitoring of activity from many areas of the in vitro and in vivo salamander olfactory bulb: a new method for studying functional organization in the vertebrate central nervous system. *J Neurosci* 1983;3:2251-2262. DOI: 10.1523/JNEUROSCI.03-11-02251.1983.
81. Kauer JS, Senseman DM, Cohen LB. Odor-elicited activity monitored simultaneously from 124 regions of the salamander olfactory bulb using a voltage-sensitive dye. *Brain Res* 1987;418:255-261. DOI: 10.1016/0006-8993(87)90093-x.
82. Pai VP, Lemire JM, Pare JF , et al. Endogenous gradients of resting potential instructively pattern embryonic neural tissue via Notch signaling and regulation of proliferation. *J Neurosci* 2015;35:4366-4385. DOI: 10.1523/JNEUROSCI.1877-14.2015.

83. Friedrich RW, Korsching SI. Combinatorial and chemotopic odorant coding in the zebrafish olfactory bulb visualized by optical imaging. *Neuron* 1997;18:737-752. DOI: 10.1016/s0896-6273(00)80314-1.
84. Friedrich RW, Korsching SI. Chemotopic, combinatorial, and noncombinatorial odorant representations in the olfactory bulb revealed using a voltage-sensitive axon tracer. *J Neurosci* 1998;18:9977-9988. DOI: 10.1523/JNEUROSCI.18-23-09977.1998.
85. Wachowiak M, Cohen LB, Zochowski MR. Distributed and concentration-invariant spatial representations of odorants by receptor neuron input to the turtle olfactory bulb. *J Neurophysiol* 2002;87:1035-1045. DOI: 10.1152/jn.00522.2001.
86. Kamino K, Komuro H, Sakai T , et al. Functional pacemaking area in the early embryonic chick heart assessed by simultaneous multiple-site optical recording of spontaneous action potentials. *J Gen Physiol* 1988;91:573-591. DOI: 10.1085/jgp.91.4.573.
87. Lee P, Quintanilla JG, Alfonso-Almazan JM , et al. In vivo ratiometric optical mapping enables high-resolution cardiac electrophysiology in pig models. *Cardiovasc Res* 2019;115:1659-1671. DOI: 10.1093/cvr/cvz039.
88. Rentschler S, Vaidya DM, Tamaddon H , et al. Visualization and functional characterization of the developing murine cardiac conduction system. *Development* 2001;128:1785-1792. DOI: 10.1242/dev.128.10.1785.
89. Tang Q, Tsytsarev V, Frank A , et al. In Vivo Mesoscopic Voltage-Sensitive Dye Imaging of Brain Activation. *Sci Rep* 2016;6:25269. DOI: 10.1038/srep25269.
90. Adams DS, Robinson KR, Fukumoto T , et al. Early, H+-V-ATPase-dependent proton flux is necessary for consistent left-right patterning of non-mammalian vertebrates. *Development* 2006;133:1657-1671. DOI: 10.1242/dev.02341.
91. Levin M, Thorlin T, Robinson KR , et al. Asymmetries in H+/K+-ATPase and cell membrane potentials comprise a very early step in left-right patterning. *Cell* 2002;111:77-89. DOI: 10.1016/s0092-8674(02)00939-x.
92. Beane WS, Morokuma J, Adams DS , et al. A chemical genetics approach reveals H,K-ATPase-mediated membrane voltage is required for planarian head regeneration. *Chem Biol* 2011;18:77-89. DOI: 10.1016/j.chembiol.2010.11.012.
93. Pezzulo G, LaPalme J, Durant F , et al. Bistability of somatic pattern memories: stochastic outcomes in bioelectric circuits underlying regeneration. *Philos Trans R Soc Lond B Biol Sci* 2021;376:20190765. DOI: 10.1098/rstb.2019.0765.
94. Rodrigues M, Leclère P, Flammang P , et al. The cellular basis of bioadhesion of the freshwater polyp Hydra. *BMC Zoology* 2016;1:1-15. DOI:
95. Gitter AH, Oliver D, Thurm U. Calcium-and voltage-dependence of nematocyst discharge in Hydra vulgaris. *Journal of Comparative Physiology A* 1994;175:115-122. DOI: 10.1007/BF00217442.
96. Steele RE. Developmental signaling in Hydra: what does it take to build a "simple" animal? *Dev Biol* 2002;248:199-219. DOI: 10.1006/dbio.2002.0744.
97. Sundelacruz S, Levin M, Kaplan DL. Depolarization alters phenotype, maintains plasticity of predifferentiated mesenchymal stem cells. *Tissue Eng Part A* 2013;19:1889-1908. DOI: 10.1089/ten.tea.2012.0425.rev.
98. Pai V, Levin M. Bioelectric controls of stem cell function. In: *Stem Cells*. Calegari F and Waskow C, eds. (CRC Press). 2013; pp. 106-148.
99. Petsakou A, Perrimon N. Bioelectric regulation of intestinal stem cells. *Trends Cell Biol* 2023;33:555-567. DOI: 10.1016/j.tcb.2022.10.003.
100. Aprea J, Calegari F. Bioelectric state and cell cycle control of Mammalian neural stem cells. *Stem Cells Int* 2012;2012:816049. DOI: 10.1155/2012/816049.

101. Levin M. Bioelectrical approaches to cancer as a problem of the scaling of the cellular self. *Prog Biophys Mol Biol* 2021;165:102-113. DOI: 10.1016/j.pbiomolbio.2021.04.007.
102. Nin V, Hernandez JA, Chifflet S. Hyperpolarization of the plasma membrane potential provokes reorganization of the actin cytoskeleton and increases the stability of adherens junctions in bovine corneal endothelial cells in culture. *Cell Motil Cytoskeleton* 2009;66:1087-1099. DOI: 10.1002/cm.20416.
103. Smithers HE, Terry JR, Brown JT , et al. Aging-Associated Changes to Intrinsic Neuronal Excitability in the Bed Nucleus of the Stria Terminalis Is Cell Type-Dependent. *Front Aging Neurosci* 2017;9:424. DOI: 10.3389/fnagi.2017.00424.
104. Thibault O, Hadley R, Landfield PW. Elevated postsynaptic [Ca2+]i and L-type calcium channel activity in aged hippocampal neurons: relationship to impaired synaptic plasticity. *J Neurosci* 2001;21:9744-9756. DOI: 10.1523/JNEUROSCI.21-24-09744.2001.
105. Chang YM, Rosene DL, Killiany RJ , et al. Increased action potential firing rates of layer 2/3 pyramidal cells in the prefrontal cortex are significantly related to cognitive performance in aged monkeys. *Cereb Cortex* 2005;15:409-418. DOI: 10.1093/cercor/bhh144.
106. Hardy CC, Al-Naggar IM, Kuo CL , et al. Aging Changes in Bladder Hyperpolarization-Activated Cyclic Nucleotide-Gated Channels Are Associated With Increasing Heterogeneity of Adrenergic/Mucosal Influence on Detrusor Control in the Mouse. *J Gerontol A Biol Sci Med Sci* 2021;76:1153-1160. DOI: 10.1093/gerona/glab070.
107. Levin M, Martyniuk CJ. The bioelectric code: An ancient computational medium for dynamic control of growth and form. *Biosystems* 2018;164:76-93. DOI: 10.1016/j.biosystems.2017.08.009.
108. Pai VP, Lemire JM, Chen Y , et al. Local and long-range endogenous resting potential gradients antagonistically regulate apoptosis and proliferation in the embryonic CNS. *The International journal of developmental biology* 2015;59:327-340. DOI: 10.1387/ijdb.150197ml.
109. Pai VP, Levin M. HCN2 channel-induced rescue of brain, eye, heart and gut teratogenesis caused by nicotine, ethanol and aberrant notch signalling. *Wound Repair Regen* 2022. DOI: 10.1111/wrr.13032.
110. Pai VP, Cervera J, Mafe S , et al. HCN2 Channel-Induced Rescue of Brain Teratogenesis via Local and Long-Range Bioelectric Repair. *Frontiers in Cellular Neuroscience* 2020;14:136. DOI: 10.3389/fncel.2020.00136.
111. Pai VP, Pietak A, Willocq V , et al. HCN2 Rescues brain defects by enforcing endogenous voltage pre-patterns. *Nat Commun* 2018;9:998. DOI: 10.1038/s41467-018-03334-5.
112. Juliano CE, Lin H, Steele RE. Generation of transgenic Hydra by embryo microinjection. *J Vis Exp* 2014:51888. DOI: 10.3791/51888.
113. Anton-Erxleben F, Thomas A, Wittlieb J , et al. Plasticity of epithelial cell shape in response to upstream signals: a whole-organism study using transgenic Hydra. *Zoology (Jena)* 2009;112:185-194. DOI: 10.1016/j.zool.2008.09.002.
114. Khalturin K, Anton-Erxleben F, Milde S , et al. Transgenic stem cells in Hydra reveal an early evolutionary origin for key elements controlling self-renewal and differentiation. *Dev Biol* 2007;309:32-44. DOI: 10.1016/j.ydbio.2007.06.013.
115. Wittlieb J, Khalturin K, Lohmann JU , et al. Transgenic Hydra allow in vivo tracking of individual stem cells during morphogenesis. *Proc Natl Acad Sci U S A* 2006;103:6208-6211. DOI: 10.1073/pnas.0510163103.
116. Braun E, Ori H. Electric-Induced Reversal of Morphogenesis in Hydra. *Biophys J* 2019;117:1514-1523. DOI: 10.1016/j.bpj.2019.09.007.